Green Chemistry

PAPER

View Article Online
View Journal | View Issue

Cite this: *Green Chem.*, 2022, **24**, 9084

Preparation of battery-grade lithium carbonate by microbubble enhanced CO_2 gas–liquid reactive crystallization†

Jijun Lu,[a,b,c] Menghua Tian,[a,b,c] Jianwei Cao,[a,b] Junhao Liu,[a,b,c] Jianwei Guo,[a,b,c] Yiwei Sun,[a,b,c] Sheng Pang,[a,b,c] Guoyu Qian*[a,b] and Zhi Wang*[a,b,c]

Lithium carbonate (Li_2CO_3), as one of the most important basic lithium salts, has a high demand in the lithium ion battery industry, including the preparation of cathode materials, lithium metal, and electrolyte additives. However, the traditional preparation process of Li_2CO_3 is hampered by the introduction of Na^+ metal impurity, and the particle size is too large to meet the requirements of battery-grade products. Here, we propose a gas–liquid reactive crystallization process for the one-step preparation of battery-grade Li_2CO_3 using CO_2 instead of Na_2CO_3 as the precipitant. This strategy avoids the introduction of Na^+ metal impurity and can also capture and convert CO_2. Meanwhile, microbubbles were introduced into the system to enhance the mass transfer and regulate the crystallization process to efficiently prepare Li_2CO_3 products with the particle size meeting the requirements of the battery level. The kinetic parameters and crystallization mechanism of battery-grade Li_2CO_3 prepared by gas–liquid reactive crystallization were quantitatively analyzed through *in situ* tests and calculations. The feasibility of using the prepared battery-grade Li_2CO_3 as a raw material to synthesize an $LiFePO_4$ cathode for lithium ion batteries was verified. The strategy provides a new route for the controllable preparation of battery-grade Li_2CO_3 and the conversion of CO_2.

Received 7th September 2022,
Accepted 17th October 2022

DOI: 10.1039/d2gc03375e

rsc.li/greenchem

Introduction

Clean energy transition and CO_2 conversion are important ways to achieve "carbon neutrality".[1,2] As one of the most significant basic lithium salts, Li_2CO_3 is used to produce lithium and other lithium compounds, such as the cathode of lithium ion batteries (LIBs), additives for electrolytes, optical devices, and medicines.[3,4] Among them, the number used in the LIB industry will account for 65% by 2025.[5] Li_2CO_3 is produced by extracting lithium from ores or salt-lake brines.[5,6] In recent years, the recycling of lithium from spent LIBs to prepare Li_2CO_3 has been regarded as an effective way to solve the shortage of lithium resources.[7–9]

However, no matter what kind of lithium resource is used as the raw material to prepare Li_2CO_3 products, Na_2CO_3 must be used as a precipitant.[10,11] This leads to the re-introduction of a large amount of Na^+ impurity. Because of the similar chemical properties of Na^+ and Li^+, it is extremely difficult to remove the Na^+ impurity. Therefore, there are few reliable ways to remove it from Li_2CO_3 products. To meet the requirement of the Na^+ content (<0.025%) for battery-grade Li_2CO_3 products, at present, it can only be partially purified by repeated washing, causticizing, carbonization, or electrolysis.[3,12,13] But the operation resulted in an extremely low recovery of Li_2CO_3 (<75%), since Li_2CO_3 is slightly soluble in water.[14] In order to obtain Li_2CO_3 products with low Na^+ content or without Na^+, it is necessary to innovate the precipitation process. What is more, battery-grade Li_2CO_3 is also required to have an average particle size of 9 μm ≤ D90 ≤ 15 μm.[15] Currently, the preparation of Li_2CO_3 by direct precipitation of a Na_2CO_3 solution belongs to a liquid–liquid mixed crystallization process with a fast reaction rate.[3] It is difficult to control, and finally the particle size of the product can hardly meet the requirements. Therefore, it is urgent to find a suitable crystallization process to replace the Na_2CO_3 precipitant, avoid the introduction of impurity metal ions, and at the same time make the crystallization process more controllable.

Preventing the introduction of impurities at the source is the most effective strategy for improving the product purity. The CO_2 gas–liquid reaction crystallization process has

[a]*CAS Key Laboratory of Green Process and Engineering, National Engineering Research Center of Green Recycling for Strategic Metal Resources, Institute of Process Engineering, Chinese Academy of Sciences, Beijing 100190, P.R. China. E-mail: gyqian@ipe.ac.cn, zwang@ipe.ac.cn*
[b]*Innovation Academy for Green Manufacture, Chinese Academy of Sciences, Beijing 100190, P.R. China*
[c]*School of Chemical Engineering, University of Chinese Academy of Sciences, Beijing 100049, P.R. China*

† Electronic supplementary information (ESI) available. See DOI: https://doi.org/10.1039/d2gc03375e

attracted great attention in the field of preparation of high-quality carbonates ($CaCO_3$, $MgCO_3$, and $BaCO_3$).[16–18] Because it has the advantage of avoiding the introduction of metal ions, and the crystallization process is more controllable. However, the slow rate of CO_2 dissolution and gas–liquid reaction crystallization seriously restricts the product conversion process of CO_2. Microbubbles can enhance the mass transfer rate, regulate the nucleation and growth kinetics, and change the crystal form and particle size of the product during the gas–liquid reaction crystallization process.[19–21] It has become an effective control method for the efficient synthesis of target products.

Here, we propose to use $NH_3{\cdot}H_2O$ and CO_2 to replace Na_2CO_3 and meanwhile regulate the gas–liquid reaction crystallization process using microbubbles for the one step preparation of Li_2CO_3 products whose purity and particle size meet the battery-grade requirements. Ammonia was introduced to provide mild alkaline conditions to avoid recrystallization and efficiently absorb CO_2. The gas–liquid reaction crystallization using CO_2 as the precipitant replaces the conventional liquid–liquid reaction system. This new strategy eliminates the introduction of Na^+ impurity, which can effectively improve the purity of Li_2CO_3 products and increase the controllability of the crystallization process. Microbubbles were introduced to enhance the gas–liquid reaction crystallization process, increasing the mass transfer rate and regulating the nucleation and growth kinetics of crystals. Finally, battery-grade Li_2CO_3 products with their purity and particle size meeting the requirements were prepared. The $LiFePO_4$ cathode was synthesized with the prepared Li_2CO_3 as the raw material. When used in lithium-ion batteries, it exhibits a remarkable electrochemical performance with an outstanding specific capacity, amazing rate capacity, and superior cyclability.

Experimental section

Synthetic battery grade Li_2CO_3 products

$NH_3{\cdot}H_2O$ (mass fraction 25–28%, analytically pure) and CO_2 (purity 99.9%) were used, without further treatment. Impurities in $NH_3{\cdot}H_2O$ and CO_2 may affect the purity of the products to some extent. Therefore, when using $NH_3{\cdot}H_2O$ and CO_2 as raw materials, their purity should be strictly controlled. The LiCl solution comes from a purified salt-lake brine or the leaching solution of spent lithium-ion battery cathodes. The LiCl solution was mixed with $NH_3{\cdot}H_2O$ to form a precursor solution (C_0 (Li^+) = 20 g L^{-1}, C_0($NH_3{\cdot}H_2O$) = 200 g L^{-1}). The temperature of the reaction solution was controlled using a thermostat. The LiCl-$NH_3{\cdot}H_2O$ mixed solution with a volume of 500 mL was poured into a reaction kettle with a double-layer glass jacket, and the stirring speed was adjusted to 400 rpm to ensure uniform mixing. The flow of CO_2 into the microbubble generator was precisely controlled using a flowmeter, and then Li_2CO_3 was prepared by the gas–liquid reaction crystallization. After the reaction, the Li_2CO_3 products collected by suction filtration were washed several times with ethanol. The Li_2CO_3 product obtained after drying was greater than 20 g.

Synthesis of the $LiFePO_4$ cathode material

$FePO_4$ (10 g, purity 99%) and Li_2CO_3 were accurately weighed in a stoichiometric ratio of 1 : 1. Then, $FePO_4$, Li_2CO_3 and glucose (20% of total mass) were mixed by ball milling at 400 rpm/min for 4 h with ethanol as the solvent. The mixture was dried (80 °C, 12 h), ground and sieved, and then calcined in an argon-protected tube furnace. Glucose was used to facilitate the synthesis of $LiFePO_4$. The Ar gas flow rate was 100 mL min^{-1}. The calcination program included pre-calcination at 300 °C for 2 h, and then the temperature was increased to 750 °C for 8 h at a heating rate of 5 °C min^{-1}. Finally, the $LiFePO_4$ cathode material was obtained.

Material characterization

pH meters (Mettler Toledo) were utilized to monitor the pH changes of the solution *in situ*. *In situ* focused beam reflectometry (FBRM, Mettler Toledo Lasentec model D600L) was used to detect the nucleation points and crystal numbers of Li_2CO_3 during crystallization. Inductively coupled plasma atomic emission spectroscopy (ICP-AES, Optima 7000DV) was performed to detect the ion content. The carbon content in the solution was detected using a total organic carbon analyzer (TOC, TOC-V CPH). The crystal forms and morphologies of the Li_2CO_3 products and the $LiFePO_4$ cathode materials were characterized using an X-ray powder diffractometer (XRD, Rigaku SmartLab 9 kW) and a scanning electron microscope (SEM, JSM-7800(Prime)), respectively. A laser particle size analyzer (Mastersizer 2000) was used to detect the particle size distribution of Li_2CO_3 crystals. The microstructures of Li_2CO_3 and $LiFePO_4$ materials were characterized by transmission electron microscopy (TEM, JEM-2100F). Thermogravimetric analysis (TG-DTA6300) was conducted to analyse the high-temperature weightlessness behavior of Li_2CO_3. X-ray photoelectron spectroscopy (XPS, Thermo Scientific K-Alpha, USA) was used to clarify the surface chemical valence states of the $LiFePO_4$ materials. The specific surface area and pore size distribution of $LiFePO_4$ were examined using the nitrogen adsorption–desorption isotherms using the Brunauer–Emmett–Teller method (Autosorb iQ).

Electrochemical testing

The electrochemical performance of the $LiFePO_4$ cathode material was characterized using a C2032-type coin cell battery. A metallic lithium sheet was used for the counter electrode. The electrode slurry was prepared by mixing $LiFePO_4$, acetylene black and polyvinylidence fluoride in *N*-methyl-2-pyrrolidone at a mass ratio of 8 : 1 : 1. Then, the mixed slurry was coated on an aluminum current collector and vacuum-dried at 80 °C for 12 h. The batteries were assembled in an Ar-filled glove box. The electrolyte consisted of 1 M $LiPF_6$ dissolved in a mixture of ethylene carbonate (EC) and diethyl carbonate (DEC) (1 : 1 in volume). The electrochemical performance was tested at voltages ranging from 2.0 to 4.0 V.

Results and discussion

Fig. 1a shows the schematic diagram of the device for the preparation of battery-grade Li_2CO_3 products by microbubble enhanced CO_2 gas–liquid reactive crystallization. The rate of CO_2 entering the reactor was precisely controlled using a gas flow meter. The pH meter was used in real time to monitor the alkalinity change of the solution in the reactor. *In situ* focused beam reflectometry (FBRM) was used to detect the nucleation sites and crystal numbers. A microbubble generator was employed to introduce microbubbles. The CO_2 gas–liquid reaction crystallization process is shown in Fig. 1b. First, CO_2 was introduced into the reactor with microbubbles to dissolve it in the liquid phase and conduct the gas–liquid mass transfer. Then, carbonate ions were provided for the crystallization process through gas–liquid and ionic reactions. When the driving force reaches the nucleation point, the Li_2CO_3 product was produced. The possible chemical reactions are described in the ESI as eqn (S1)–(S6).†

In order to verify the feasibility of preparing Li_2CO_3 using the LiCl-NH_3·H_2O-CO_2 system, the equilibrium constants and thermodynamic parameters of the reaction in eqn (1) and (2) were calculated using the HSC Chemistry software. The calculation results are shown in Table S1† and Fig. 1c. The comparison shows that both reactions can proceed spontaneously, but compared with reaction (2), formula (1) has the following advantages: (i) it has a larger absolute value of Gibbs free energy, and the reaction is more likely to occur. (ii) Eqn (1) shows that the exothermic reaction has more advantages in thermodynamics. (iii) The equilibrium constant of reaction (1) is much larger than that of reaction (2) in theory, making reaction (1) more thorough. In conclusion, it is feasible to prepare Li_2CO_3 products by gas–liquid reaction crystallization of the LiCl-NH_3·H_2O-CO_2 system.

$$2LiCl + 2NH_3 \cdot H_2O + CO_2 \leftrightarrow Li_2CO_3(s) + 2NH_4Cl + H_2O \quad (1)$$

$$2LiCl + Na_2CO_3 \leftrightarrow Li_2CO_3(s) + 2NaCl \quad (2)$$

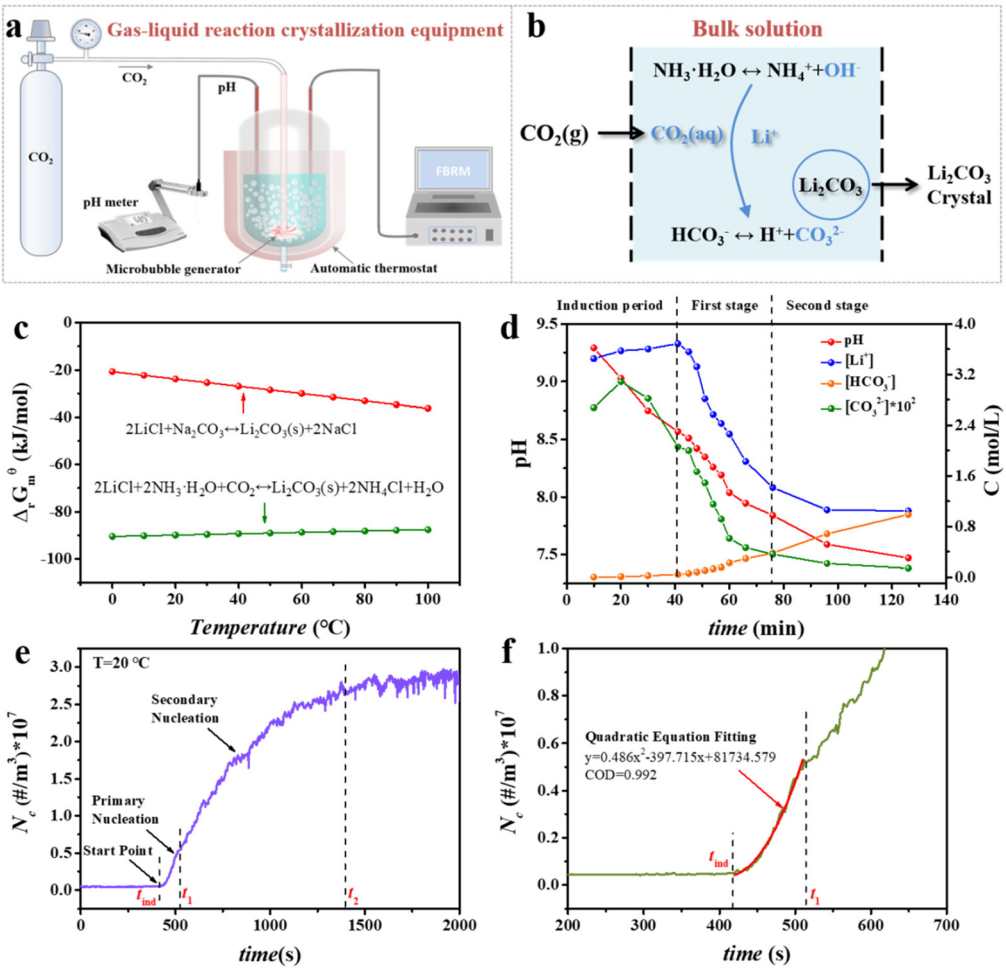

Fig. 1 (a) Microbubble-controlled reaction crystallization device in the LiCl-NH_3·H_2O-CO_2 system. (b) Schematic diagram of the gas–liquid reaction crystallization process. (c) Thermodynamic comparison between the new process and the traditional reaction. (d) The three stages of Li_2CO_3 production in the LiCl-NH_3·H_2O-CO_2 system and the changes of various parameters. (e) Different stages of nucleation. (f) Quadratic equation regression calculation.

Inductively coupled plasma atomic emission spectrometry (ICP-AES) and a total organic carbon analyzer (TOC) were used to detect changes in the concentration of species in the solution during the reaction. Subsequently, the parameters of the gas–liquid reaction crystallization process were mastered by calculating the concentrations of Li^+, HCO_3^- and CO_3^{2-}, and the detailed calculation process is described in the ESI.† Fig. 1d shows the changes in the pH and ion concentration in solution during the gas–liquid reaction crystallization. The generation of the Li_2CO_3 product can be divided into three stages: (i) during induction, the Li^+ concentration remains unchanged. (ii) In the first stage of crystallization, the Li^+ concentration decreases linearly and rapidly. (iii) In the second stage of crystallization, the Li^+ concentration decays slowly. The decreasing rate of Li^+ concentration reflects the crystallization speed of Li_2CO_3. The pH of the solution decreased linearly throughout the reaction process until a pH value of about 7.6 was reached at the end of crystallization. The concentration of HCO_3^- increases continuously in the crystallization process. The concentration of CO_3^{2-} ions increased briefly and then decreased, and the decreasing trend was consistent with the change in the Li^+ concentration. The concentration of CO_3^{2-} ions was two orders of magnitude smaller than that of HCO_3^-. As the pH of the solution was relatively low, reaction (S2)† predominated, with reaction (S3) and (S5)† occurring only infrequently.

CO_2 dissolves continuously (reactions (S1) and (S2)†) during the gas–liquid crystallization. Since the dissolved CO_2 was continuously converted into HCO_3^-, the HCO_3^- concentration remains constant in the crystallization process. In addition, there was an important phenomenon for the preparation of Li_2CO_3 from the LiCl-NH_3·H_2O-CO_2 system. Throughout the crystallization process, the Li^+ concentration decreased continuously, and no re-dissolution of Li_2CO_3 crystals occurred. This indicates that the LiCl-NH_3·H_2O-CO_2 system can inhibit the recrystallization of Li_2CO_3 crystals and avoid excessive carbonization. Thus, a larger Li_2CO_3 yield could be obtained, compared to the strong base system of LiOH/KOH-CO_2.[3,22]

Mastering the nucleation and growth rate of Li_2CO_3 crystals in the crystallization process can effectively control the crystal form and particle size of the product. To obtain the nucleation rate of the Li_2CO_3 crystallization process, *in situ* FBRM was used to detect the change in the number of crystal particles per unit volume and time. The nucleation rate was then calculated using eqn (S16).† The progression from the point of nucleation (t_{ind}) to the apparent change in the number of crystal grains (t_1) was called primary nucleation (Fig. 1e). The changing process of the particle number from t_1 to the second turning point t_2 was secondary nucleation. By fitting the primary nucleation process (Fig. 1f), showing that its particle number varies linearly with time, the average nucleation rate can be calculated using eqn (S17).†

The nucleation rates of Li_2CO_3 at different temperatures are shown in Fig. 2a. The nucleation rate increases gradually as the temperature increases from 25 °C to 50 °C. At temperatures above 50 °C, the crystallization rate remains stable. This could be explained by the change in the supersaturation of the solution (Fig. 2b). The supersaturation of the solution was extremely low (<1.6) at 60 °C, resulting in a critical nucleation size of Li_2CO_3.[3] This makes the nucleation conditions more stringent, which was not conducive to the nucleation process, thus limiting the further improvement of the nucleation rate by temperature. As a result, eqn (S18)–(S20)† could be used to express the kinetics of nucleation from 20 °C to 50 °C. The nucleation activation energy could be determined using the relationship between the temperature and the nucleation rate, as shown in Fig. 2c. The large nucleation activation energy (79.15 kJ mol^{-1}) shows that the temperature has a greater effect on the nucleation rate, and the nucleation process was believed to be controlled by surface reactions.

The effects of different supersaturations on the nucleation rate at 50 °C are shown in Fig. 2d and e. The nucleation rate increases with the increase in supersaturation. The reaction order could be calculated using the relationship between the supersaturation and the nucleation rate (S18).†[23] As shown in Fig. 2f, the calculated result of the nucleation rate series was 6.81, indicating that the nucleation rate was greatly affected by the supersaturation. Therefore, the grain size of the Li_2CO_3 crystals can be directionally controlled by regulating the supersaturation degree of the nucleation process. By fitting the relationship between the nucleation rate and the supersaturation (Fig. 2g), an interfacial energy of 22.03 mJ m^{-2} could be obtained using eqn (S21).† Fig. 2h shows the relationship between the induction period and supersaturation. Combining the formula (S22),† the interfacial energy can be calculated as 18.8 mJ m^{-2}. The interfacial energies obtained by the above two methods were close, representing that the method of using FBRM to calculate the nucleation rate was reasonable. Based on the relationship between the growth rate and the temperature, the growth activation energy of Li_2CO_3 could be calculated using the formula (S23),† as shown in Fig. 2i. The growth activation energy of the Li_2CO_3 crystal was 26.79 kJ mol^{-1}, which was lower than the nucleation activation energy (79.15 kJ mol^{-1}). This denotes that the energy barrier of the growth process was lower than that of the nucleation process, and the temperature had little effect on the growth. In summary, the particle size of the Li_2CO_3 crystals can be reduced in two aspects: (i) increasing the supersaturation of the system to promote the production of more Li_2CO_3 crystals per unit time and (ii) slowing down its rate of growth.

The crystal form of the Li_2CO_3 product is shown in Fig. 3a, and its diffraction peak is consistent with the standard PDF (No. 83-1454). No impurity peaks were found in the spectrum, indicating that the obtained Li_2CO_3 product was of high purity. The particle size distribution of the Li_2CO_3 product obtained under mechanical stirring is shown in Fig. 3b. D90 was about 32.5 μm, which is larger than the requirement of battery-grade Li_2CO_3 (9 μm ≤ D90 ≤ 15 μm). Its microscopic morphology is shown in Fig. 3c, with flower-like clusters formed by sheet-like monomers. In order to reduce the particle size of the Li_2CO_3 crystals to meet the requirements of battery-

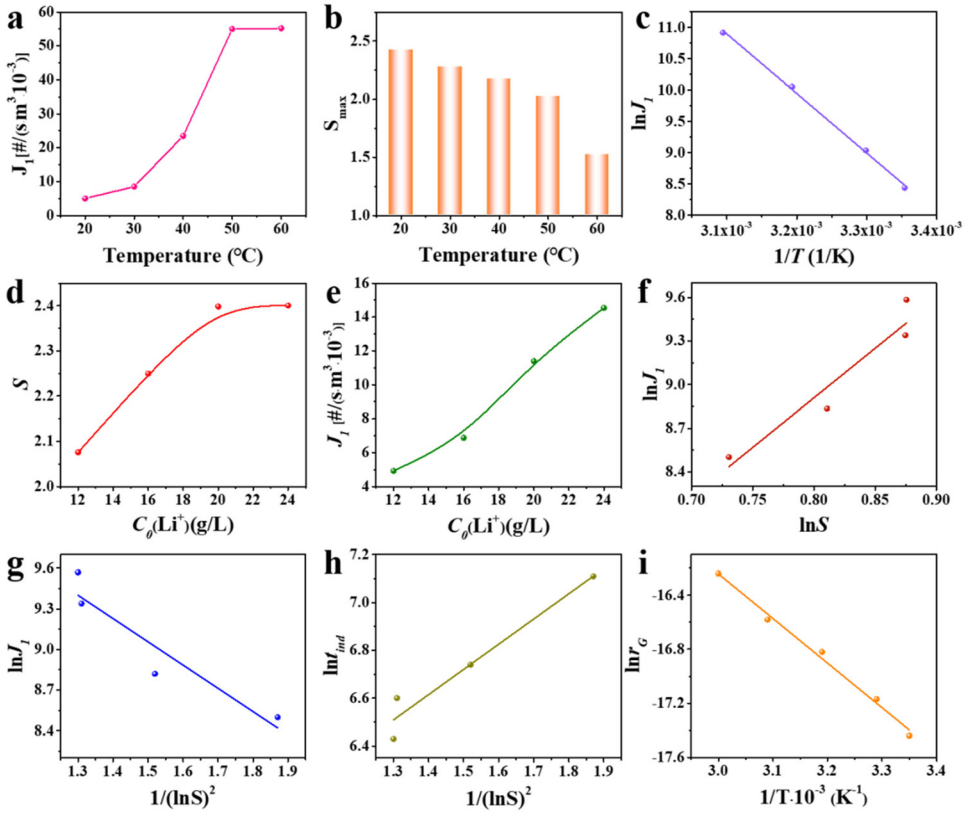

Fig. 2 Nucleation and growth kinetics of the Li_2CO_3 crystal. Relationship between the temperature and (a) the nucleation rate and (b) the maximum supersaturation. (c) Calculation of the nucleation activation energy. (d) Relationship between the initial Li^+ concentration and the supersaturation and (e) the nucleation rate. (f and g) Nucleation rate *versus* supersaturation. (h) Induction period as a function of supersaturation. (i) Growth rate *versus* temperature.

grade products, microbubbles were introduced to regulate the nucleation and growth process of Li_2CO_3 crystals.

The particle size distribution of the Li_2CO_3 product after the introduction of microbubbles is shown in Fig. 3d. After 180 min of reaction, the particle size of Li_2CO_3 obtained at 25 °C ranges from 13 to 17 μm and D90 was about 14.6 μm. Its microscopic morphology was a spherical flower-like structure (Fig. 3e). To confirm the effect of microbubbles on the particle size reduction, normal bubble experiments were carried out, and the results are shown in Fig. S1.† The particle size was D90 ≈ 30 μm after 80 min of reaction. Thermogravimetric analysis (TGA) is shown in Fig. S2,† and there was an endothermic dehydration phenomenon in the Li_2CO_3 products. Its weight loss was attributed to the removal of crystal water. The key role of microbubbles was analyzed by FBRM to detect the chord length evolution law of the crystallization process with or without microbubbles (Fig. 3f and g). Fig. S3† shows the chord length distribution of carbonized crystallization at 200 s and 400 s with or without microbubbles. At this time, the solution was still in the induction stage and no crystals were formed. Without microbubbles, the chord length had no obvious distribution peak. Under the conditions of introducing microbubbles, Li_2CO_3 had an obvious chord length distribution peak before crystallization, and the width was in the range of 1–50 μm. It shows that the chord length distribution range detected by FBRM was the size of the microbubble (1–50 μm).

The dotted line represents the chord length distribution of the microbubbles, and the solid line represents the chord length distribution of the grains. Initially, the chord length distribution shows that particles larger than 10 μm predominate in the absence of microbubbles. In the presence of microbubbles, the chord length distribution of the crystal particles was approximately 10 μm consistent with the microbubbles (Fig. 3f). As the crystallization reaction progresses, the chord length distribution peak gradually shifts to the left, indicating that the particle size decreases. However, after 5500 s of reaction, a small amount of large-sized (~50 μm) Li_2CO_3 crystals were formed in the system. This may be due to the agglomeration of the formed Li_2CO_3 crystals. Therefore, it is necessary to control the crystallization time in the process of microbubble-controlled gas–liquid reaction crystallization to obtain battery-grade Li_2CO_3 products.

We speculate that the main reasons for the reduction in the particle size of Li_2CO_3 by microbubbles are as follows: (i) microbubbles increase the gas–liquid interface, which enhances mass transfer and CO_2 absorption, as well as the local supersaturation and the nucleation process. (ii) Reaction micro-regions can be formed near the gas–liquid interface of

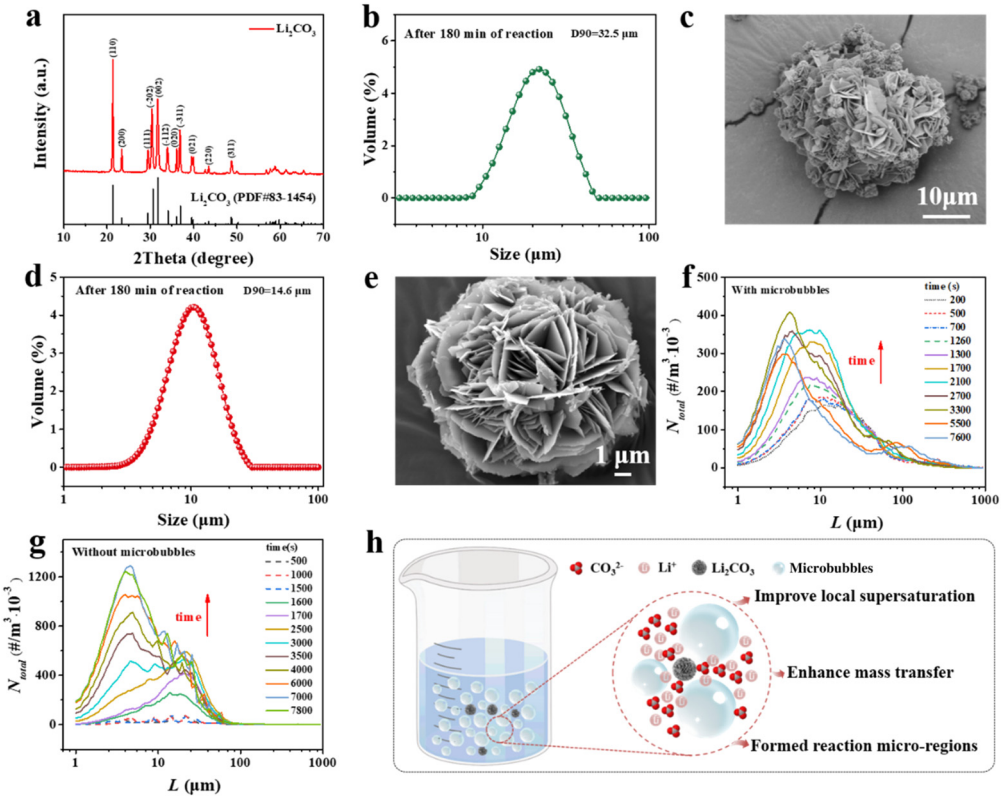

Fig. 3 Physicochemical properties of the Li_2CO_3 crystals synthesized without microbubbles. (a) The X-ray diffraction (XRD) pattern. (b) The particle size distribution. (c) The scanning electron microscopy (SEM) image. (d and e) The particle size distribution and SEM image of Li_2CO_3 prepared with microbubbles. The chord length distribution of the Li_2CO_3 crystallization process (f) with microbubbles and (g) without microbubbles. (h) Mechanism of microbubble regulating gas–liquid reaction crystallization process.

microbubbles to inhibit the growth of crystals. The mechanism of promotion of nucleation and restraining growth by microbubbles is shown in Fig. 3h. Based on the above analysis, the mechanism for preparing Li_2CO_3 by gas–liquid reaction crystallization of the LiCl-$NH_3{\cdot}H_2O$-CO_2 system is shown in Fig. 4. The crystallization process can be divided into four steps: (1) OH^- was dissociated by $NH_3{\cdot}H_2O$. (2) The dissolution of CO_2 results in the formation of HCO_3^-. (3) HCO_3^- reacts with OH^- to generate CO_3^{2-}. (4) CO_3^{2-} reacts with Li^+ to form the Li_2CO_3 crystals. Not only was there no introduction of impurity metal ions in the whole system, but it can also absorb CO_2 for productization.

Due to its environmental friendliness, relative safety and strong stability, $LiFePO_4$ has been widely used as a cathode material for lithium-ion power batteries.[24–26] The feasibility of preparing lithium-ion battery cathode materials with the obtained battery-grade Li_2CO_3 was verified. The XRD pattern shows that the characteristic peaks of the prepared $LiFePO_4$ are consistent with the standard phase (No. 81-1173) (Fig. 5a).[27] $LiFePO_4$ delivered a sphere-like structure with a par-

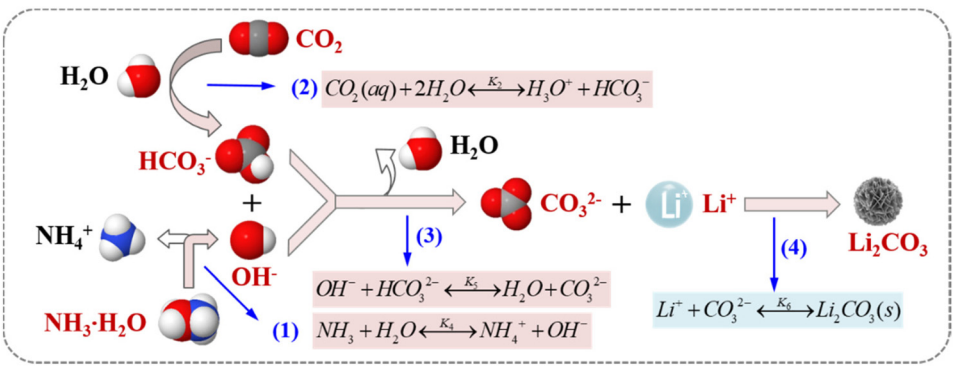

Fig. 4 The mechanism of the reaction crystallization process of the LiCl-$NH_3{\cdot}H_2O$-CO_2 system.

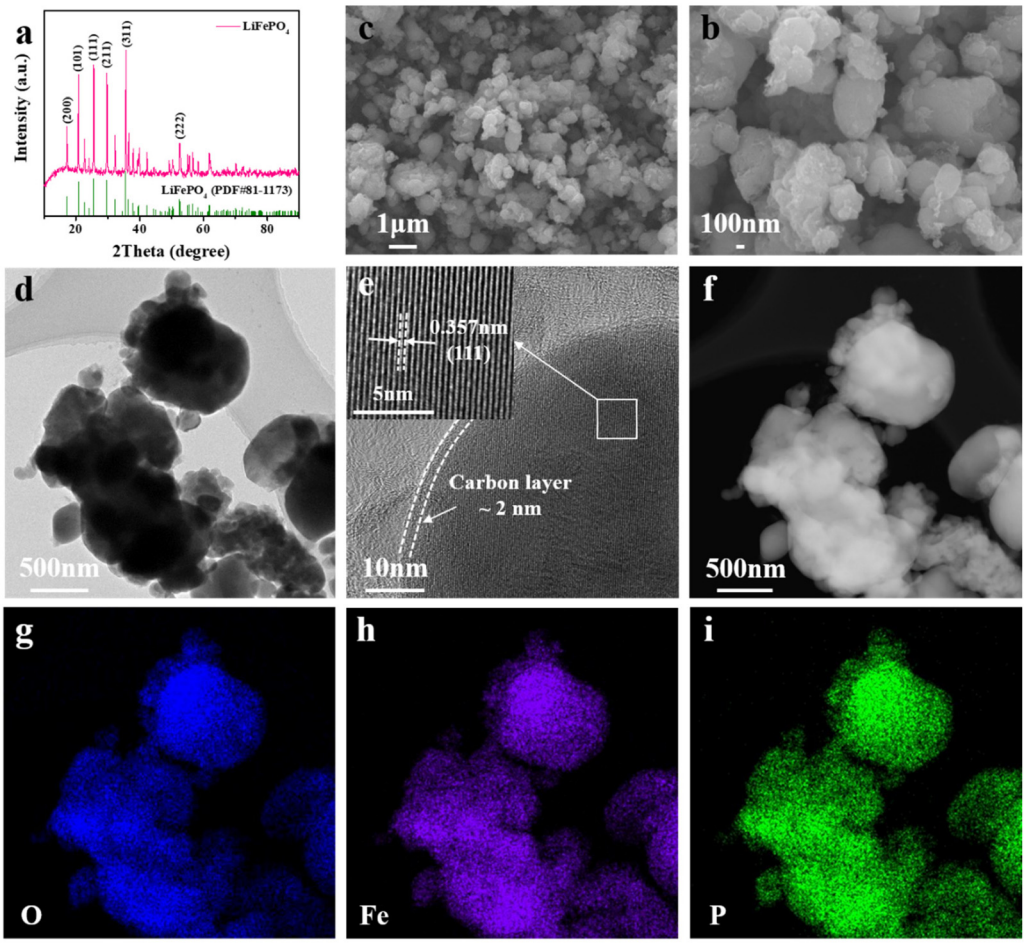

Fig. 5 Physical and chemical characteristics of the $LiFePO_4$ cathode materials. (a) The XRD pattern. (b and c) SEM images at different magnifications. (d) The transmission electron microscopy (TEM) image. (e) The high-resolution TEM (HRTEM) image. (f) The high-angle annular dark-field scanning transmission electron microscopy (HAADF-STEM) image. (g–i) Energy dispersive spectroscopy (EDS) mapping images.

ticle size of about 1 μm (Fig. 5b and c). The small particle size is conducive to the rapid de-intercalation of lithium ions in the core of the $LiFePO_4$ material. The wrinkled protrusions on the particle surface are carbon layers formed by glucose carbonization. The TEM images show that the $LiFePO_4$ cathode material has a core–shell structure, and the outer layer is wrapped by an amorphous carbon layer of about 2 nm (Fig. 5d and e). The presence of the carbon layer can hinder the further growth of $LiFePO_4$ particles.[28] The formation of the composite material contributes to the improvement of the electronic conductivity of the $LiFePO_4$ cathode. The inset shows a regular crystal structure at the core. The lattice fringe spacing of 0.357 nm corresponds to the (111) crystal plane of $LiFePO_4$.[29] HAADF-STEM and EDS mapping were performed to analyze the elemental composition and distribution of the $LiFePO_4$ materials, as shown in Fig. 5f–i.

X-ray photoelectron spectroscopy (XPS) analysis showed that the $LiFePO_4$ material was mainly composed of Fe, C, P, Li, and O elements (Fig. 6a). The high-resolution C 1s spectracorrespond to C–O, C═O, and C–C bonds, respectively (Fig. 6b).[30] The Fe 2p map shows characteristic peaks located at 724.5 eV and 710.3 eV attributed to Fe^{2+} (Fig. 6c).[29,31] The P 2p spectrum at 133.6 eV corresponds to the P–O bond (Fig. 6d).[32] It was confirmed that the $LiFePO_4$ cathode material was controllably synthesized. The specific surface area and pore size distribution of the $LiFePO_4$ samples were characterized using nitrogen adsorption–desorption tests, as shown in Fig. 6e and f, with typical type IV isotherms and type-H3 hysteresis loops. Their specific surface area is 9.75 mg cm^{-2}. The existence of micropores facilitates the rapid diffusion of lithium ions and the fluctuation of the released volume.

The electrochemical performance of the $LiFePO_4$ cathode was tested in the voltage range of 2.0–4.0 V at 25 °C. The schematic diagram of the charging and discharging process of the lithium-ion battery is shown in Fig. 7a; the counter electrode is the Li metal. The voltage–capacity curve shows that the prepared $LiFePO_4$ cathode has an initial coulombic efficiency (ICE) of 96.68% and an average capacity loss of 0.068% per cycle (Fig. 7b). Its average operating voltage is 3.42 V. Fig. 7c and d show that the $LiFePO_4$ cathode delivered an outstanding rate capability and still possessed a specific capacity of 135.8 mA h g^{-1} at a rate of 2.5C (a capacity retention rate of

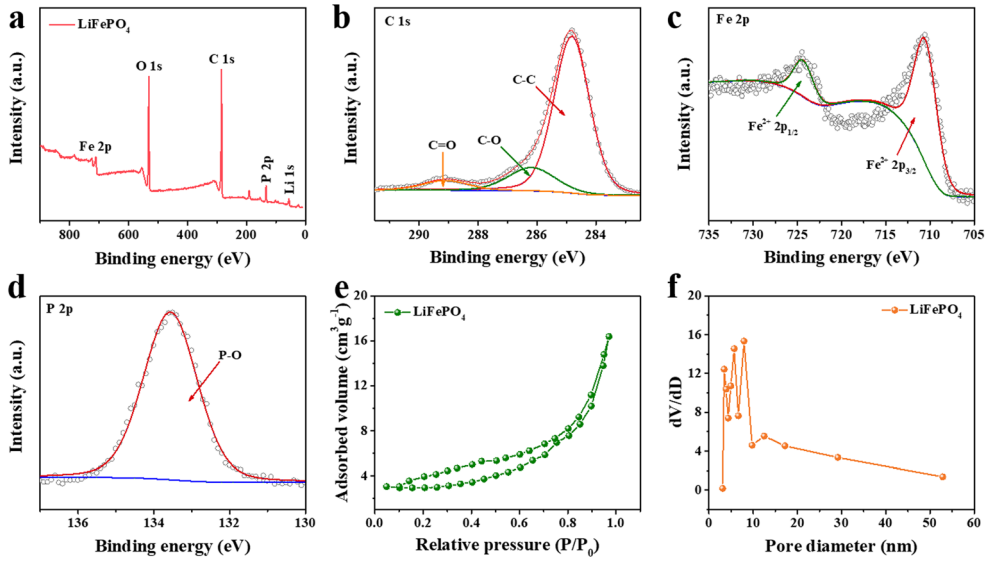

Fig. 6 Characterization of the $LiFePO_4$ samples. (a)The full spectrum of XPS. High-resolution XPS spectra of (b) C 1s, (c) Fe 2p, and (d) P 2p. (e) Nitrogen adsorption–desorption isotherms. (f) Pore size distribution.

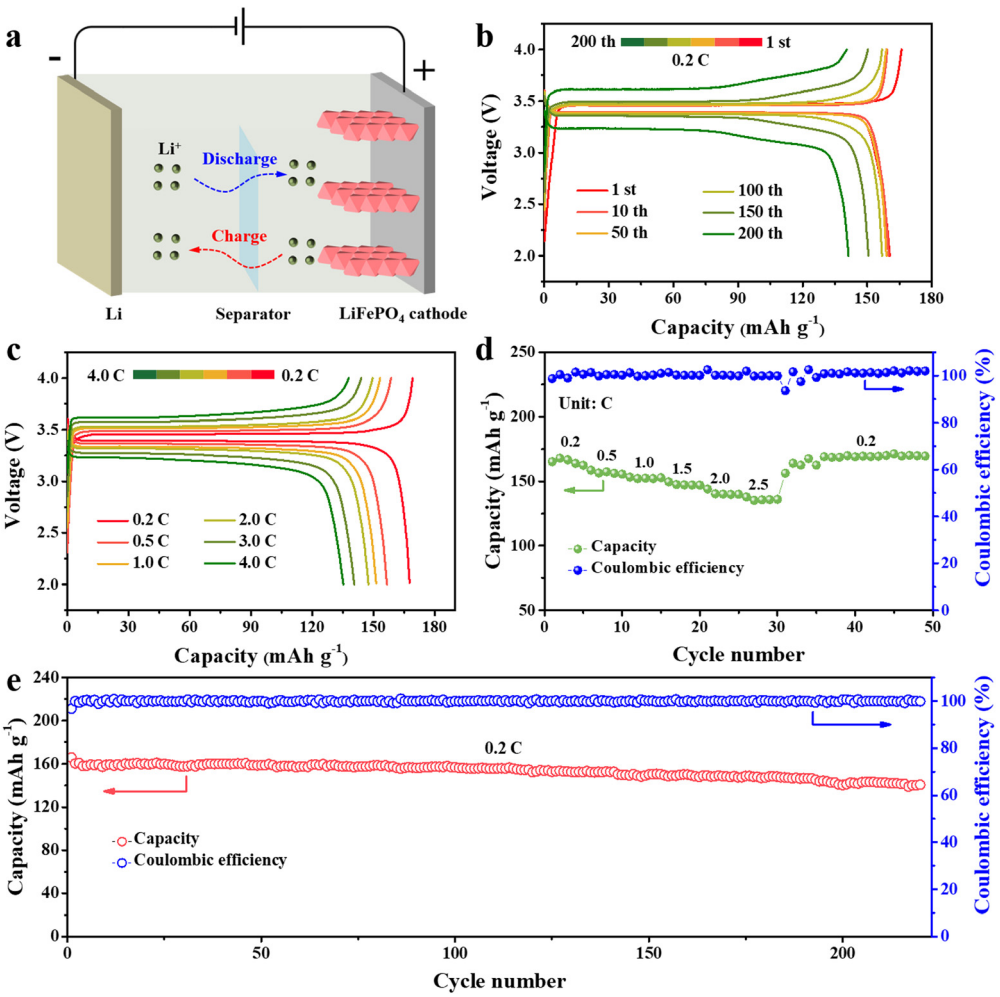

Fig. 7 The electrochemical performance of the $LiFePO_4$ cathode. (a) Schematic diagram of a lithium-ion battery. (b) Typical capacity–voltage curves at a rate of 0.2C. (c) Charge–discharge curves at the rate increasing from 0.2C to 2.5C. (d) Rate performance. (e) Long cycling stability at a rate of 0.2C.

82.2%). The $LiFePO_4$ cathode shows excellent long cycling stability (Fig. 7e) with a reversible specific capacity of 140.7 mA h g^{-1} at a rate of 0.2C for 220 cycles (>85% of the original capacity retention). Compared with the previously reported work, it exhibits a superior electrochemical performance even under the conditions of bare $LiFePO_4$ cathodes (Fig. S4 and Table S2†). The superior electrochemical performance of the $LiFePO_4$ cathode material prepared from battery-grade Li_2CO_3 was demonstrated. It was verified that the battery-grade Li_2CO_3 products prepared using the LiCl-NH_3·H_2O-CO_2 system are feasible to be applied to lithium-ion batteries.

Conclusion

In conclusion, we propose a novel strategy for the controllable and efficient preparation of battery-grade Li_2CO_3. In this strategy, CO_2 was converted into CO_3^{2-} in NH_3·H_2O solution to replace the traditional Na_2CO_3 as a precipitant. Meanwhile, microbubbles were introduced into the system to enhance the gas–liquid mass transfer and CO_2 absorption, improve local supersaturation, and form reaction micro-zones. The results show that using CO_2 as a precipitant to prepare Li_2CO_3 not only avoids the introduction of impurity metal ions, but can also convert CO_2 into products. What is more, the LiCl-NH_3·H_2O-CO_2 system belongs to the weak base system, which can inhibit the recrystallization of Li_2CO_3. The particle size of Li_2CO_3 decreased significantly with the introduction of microbubbles, and D90 decreased from 32.5 μm to 14.6 μm. This is mainly attributed to the fact that the increase in the local supersaturation, which can promote nucleation, and the formation of reactive micro-zones can inhibit the crystal growth. Therefore, a Li_2CO_3 product whose purity and particle size meet the battery-grade requirements has been obtained. The $LiFePO_4$ cathode synthesized from the currently prepared Li_2CO_3 product exhibits a remarkable long cycling stability (>85% of the original capacity retention) and superior rate capability (135.8 mA h g^{-1} at a rate of 2.5C). The successful application of this method will contribute to the rapid development of the lithium-ion power battery industry and the early realization of "carbon neutrality".

Author contributions

J. L. and Z. W. conceived the strategy and designed the experiments. J. L. and M. T. carried out experiment preparation, material characterization, data analysis and original manuscript draft writing. S. P., and J. L. prepared the electrode materials and conducted electrochemical measurements. J. C., J. G. and Y. S. performed the theoretical calculations. G. Q. and Z. W. supervised the project, discussed the results and revised the manuscript. All authors discussed the results and commented on the manuscript.

Conflicts of interest

There are no conflicts to declare.

Acknowledgements

This work was partially funded by the Key Program of Chinese Academy of Sciences (ZDRW_CN_2020-1) and the National Natural Science Foundation of China (51934006 and 52074255).

References

1 I. Sullivan, A. Goryachev, I. A. Digdaya, X. Li, H. A. Atwater, D. A. Vermaas and C. Xiang, *Nat. Catal.*, 2021, **4**, 952–958.
2 N. Zhao and F. You, *Appl. Energy*, 2020, **279**, 115889.
3 Y.-Z. Sun, X.-F. Song, M.-M. Jin, W. Jin and J.-G. Yu, *Ind. Eng. Chem. Res.*, 2013, **52**, 17598–17606.
4 S. Klein, P. Harte, J. Henschel, P. Bärmann, K. Borzutzki, T. Beuse, S. Wickeren, B. Heidrich, J. Kasnatscheew, S. Nowak, M. Winter and T. Placke, *Adv. Energy Mater.*, 2021, **11**, 2003756.
5 M. Lee, W. Jung, H. J. Kwon and G. Lim, *J. Mater. Chem. A*, 2022, **10**, 4621–4633.
6 J. Yu, M. Zheng, Q. Wu, Z. Nie and L. Bu, *Sol. Energy*, 2015, **115**, 133–144.
7 X. Qiu, B. Zhang, Y. Xu, J. Hu, W. Deng, G. Zou, H. Hou, Y. Yang, W. Sun, Y. Hu, X. Cao and X. Ji, *Green Chem.*, 2022, **24**, 2506–2515.
8 J. Zhang, G. Liang, C. Yang, J. Hu, Y. Chen and C. Wang, *Green Chem.*, 2021, **23**, 8434–8440.
9 J. Lin, C. Liu, H. Cao, R. Chen, Y. Yang, L. Li and Z. Sun, *Green Chem.*, 2019, **21**, 5904–5913.
10 N. Linneen, R. Bhave and D. Woerner, *Sep. Purif. Technol.*, 2019, **214**, 168–173.
11 B. Swain, *Sep. Purif. Technol.*, 2017, **172**, 388–403.
12 W. Yi, C. Yan, P. Ma, F. Li and X. Wen, *Sep. Purif. Technol.*, 2007, **56**, 241–248.
13 Z. Zhou, F. Liang, W. Qin and W. Fei, *Ind. Eng. Chem. Res.*, 2014, **60**, 282–288.
14 D. Liu, Z. Zhao, W. Xu, J. Xiong and L. He, *Desalination*, 2022, **519**, 115302.
15 W. Liu, G.-W. Chu, S.-C. Li, S. Bai, Y. Luo, B.-C. Sun and J.-F. Chen, *Chem. Eng. J.*, 2019, **377**, 119929.
16 P. Chen, S. Tang, H. Yue, C. Liu, C. Li and B. Liang, *Ind. Eng. Chem. Res.*, 2017, **56**, 5668–5678.
17 W.-M. Jung, S.-H Kang, K.-S. Kim, W.-S. Kim and C.-K Choi, *J. Cryst. Growth*, 2010, **312**, 3331–3339.
18 P.-C. Chen, S. M. Liu, C. J. Jang, R. C. Hwang, Y. L. Yang, J. S. Lee and J. S. Jang, *J. Cryst. Growth*, 2003, **257**, 333–343.
19 J.-H. Bang, Y. N. Jang, W. Kim, K. S. Song, C. W. Jeon, S. C. Chae, S.-W. Lee, S.-J. Park and M. G. Lee, *Chem. Eng. J.*, 2012, **198–199**, 254–260.

20 M. Matsumoto, M. Ohno, Y. Wada, T. Sato, M. Okada and T. Hiaki, *J. Cryst. Growth*, 2017, **469**, 91–96.
21 Y. Tsuchiya, Y. Wada, T. Hiaki, K. Onoe and M. Matsumoto, *J. Cryst. Growth*, 2017, **469**, 36–41.
22 Y. Jiang, C. Liu, X. Zhou, P. Li, X. Song and J. Yu, *Energy Sources, Part A*, 2019, **43**, 3332–3344.
23 J. Li, C. A. Prestidge and J. Addai-Mensah, *J. Colloid Interface Sci.*, 2000, **224**, 317–324.
24 L. Guo, Y. Zhang, J. Wang, L. Ma, S. Ma, Y. Zhang, E. Wang, Y. Bi, D. Wang, W. C. McKee, Y. Xu, J. Chen, Q. Zhang, C. Nan, L. Gu, P. G. Bruce and Z. Peng, *Nat. Commun.*, 2015, **6**, 7898.
25 J. Li and Z.-F. Ma, *Chem*, 2019, **5**, 3–6.
26 Q. Fan, Y. Zhang, Q. Xu, J. Wang, L. Lei, Y. Sun and P. D. Lund, *Energy Stor. Mater.*, 2019, **21**, 457–463.
27 Y. Mo, J. Liu, C. Meng, M. Xiao, S. Ren, L. Sun, S. Wang and Y. Meng, *Carbon*, 2019, **147**, 19–26.
28 B. Wang, D. Wang, Q. Wang, T. Liu, C. Guo and X. Zhao, *J. Mater. Chem. A*, 2013, **1**, 135–144.
29 X. Wang, Z. Feng, X. Hou, L. Liu, M. He, X. He, J. Huang and Z. Wen, *Chem. Eng. J.*, 2020, **379**, 122371.
30 B. Wang, W. Al Abdulla, D. Wang and X. S. Zhao, *Energy Environ. Sci.*, 2015, **8**, 869–875.
31 Y. Song, B. Xie, S. Song, S. Lei, W. Sun, R. Xua and Y. Yang, *Green Chem.*, 2021, **23**, 3963–3971.
32 J. Lin, Y.-H. Sun and X. Lin, *Nano Energy*, 2022, **91**, 106655.